Giant orbital magnetoresistance in the antiferromagnet CoO driven by dynamic orbital angular momentum interaction

Christin Schmitt[1], Sachin Krishnia[1,*], Mahmoud Zeer[2], Edgar Galíndez-Ruales[1], Mehak Loyal[1], Jonas Köhler[1], Luca Micus[1], Takashi Kikkawa[3,4], Hiroki Arisawa[3,5], Thibaud Denneulin[6], András Kovács[6], Renyou Xu[1,7], Duc Tran[1], Florian Kronast[8], Dongwook Go[1,2,9], Leonid V. Pourovskii[10,11], Rafal E. Dunin-Borkowski[6], Timo Kuschel[1,12], Marjana Ležaić[2], Jairo Sinova[1,13], Eiji Saitoh[3,5,14,15], Gerhard Jakob[1], Olena Gomonay[1], Yuriy Mokrousov[1,2], Mathias Kläui[1,16,*]

[1]Institute of Physics, Johannes Gutenberg-University Mainz, 55128 Mainz, Germany.

[2]Peter Grünberg Institut and Institute for Advanced Simulation, Forschungszentrum Jülich and JARA, 52425 Jülich, Germany.

[3]Department of Applied Physics, The University of Tokyo,113-8656 Tokyo, Japan.

[4]Advanced Science Research Center, Japan Atomic Energy Agency, 319-1195 Tokai, Japan.

[5]RIKEN Center for Emergent Matter Science, 0351-0198 Wako, Japan.

[6]Ernst Ruska-Centre for Microscopy and Spectroscopy with Electrons, Forschungszentrum Jülich, 52425 Jülich, Germany.

[7]Fert Beijing Institute, MIIT Key Laboratory of Spintronics, School of Integrated Circuit Science and Engineering, Beihang University, 100191 Beijing, China.

[8]Helmholtz-Zentrum Berlin für Materialien und Energie, 12489 Berlin, Germany.

[9]Department of Physics, Korea University, Seoul 02841, Republic of Korea.

[10] CPHT, CNRS, École polytechnique, Institut Polytechnique de Paris, 91120 Palaiseau, France.

[11] Collège de France, Université PSL, 11 place Marcelin Berthelot, 75005 Paris, France.

[12]Faculty of Physics, Bielefeld University, 33615 Bielefeld, Germany.

[13]Department of Physics, Texas A&M University, College Station, Texas 77843-4242, USA.

[14]WPI-Advanced Institute for Materials Research, Tohoku University, 980-8577 Sendai, Japan.

[15]Institute for AI and Beyond, The University of Tokyo, 113-8656 Tokyo, Japan.

[16]Center for Quantum Spintronics, Norwegian University of Science and Technology, 7491 Trondheim, Norway.

*Corresponding authors. Email: skrishni@uni-mainz.de, klaeui@uni-mainz.de

Recent predictions of orders of magnitude larger orbital current effects compared to spin currents have attracted significant interest. However, the potential of giant orbital currents remains underutilized, as they must first be converted into spin currents to interact with the static magnetization dominated by spin angular momentum in conventional magnets. By using a magnet dominated by orbital angular momentum, we demonstrate a seventy-fold enhancement in orbital Hall magnetoresistance in CoO/Cu*, compared to CoO/Pt. This arises from unique interactions between dynamic orbital angular momentum from surface oxidized Cu* (i.e., the orbital current) and static orbital angular momentum in the antiferromagnetic insulator CoO. Our results show how by using orbital angular momentum-dominated materials, we can harness the benefits of giant orbital currents that have not been possible using conventional spin-dominated magnets, for orbitronics-based devices, offering unprecedented energy efficiency for operations of antiferromagnets that combine ultimate stability with THz dynamics.

Introduction

In recent decades, the interaction between static magnetization and the flow of spin angular momentum (spin currents), has been employed as the key mechanism to detect and control the magnetic state of ferromagnets. This interaction has enabled major applications, ranging from giant magnetoresistance sensors (*1, 2*) to spin-orbit torque magnetic random-access memory (*3, 4*), chiral skyrmion-based racetrack memory (*5, 6*), logic devices (*7*), and neuromorphic applications (*8–10*). However, the generation of spin current relies heavily on the spin-orbit coupling (SOC) of the materials, which is a weak relativistic effect that limits the efficiency and constrains materials choices (*11*).

More recently, the dynamic orbital angular momentum (OAM) – the counterpart of electron spin angular momentum – has emerged as a promising alternative to manipulate magnetization more efficiently (*12–15*). Two mechanisms of orbital current generation are orbital Hall effect (OHE) in the bulk (*13, 16, 17*) and orbital Rashba Edelstein effect (OREE) at interfaces (*18, 19*), analogous to those of spin current generation (*20*). Unlike spin currents, whose generation from charge currents relies on the relatively weak SOC mechanism, orbital currents can be directly generated from charge currents because the crystal momentum of charge carriers (e.g. electrons) can directly couple to OAM. This results in a more robust, orders-of-magnitude larger generation of current-induced OAM (orbital currents), even in light, abundant, inexpensive and environmentally friendly materials (*13, 21–25*). Despite these advantages, the fundamental limitation in utilizing orbital currents for device applications lies in their low interaction efficiency with magnetization that in conventional transition metals is carried by spin angular momentum. While spin currents interact efficiently with magnetization (or spin moments) via strong *s-d* exchange interaction, orbital currents cannot couple in conventional magnetic materials with nearly quenched OAM by any strong exchange interaction and, therefore, one cannot make use of the large orbital currents to effectively interact with conventional spin-based magnets.

To address this issue of inefficient interaction with conventional magnets, the mitigation strategy has been the conversion of orbital currents into spin currents using materials that exhibit high SOC (*14, 26*). However, the efficiency in such cases again relies on the comparably weak relativistic SOC mechanism in the conversion layer. Although this approach achieves a modest enhancement

in spin torque efficiency, typically a fewfold (*14, 27–29*), it remains significantly smaller than the theoretically predicted orders of magnitude enhancement.

Thus, to fully exploit the potential of large orbital currents, one needs to directly couple it with orbital magnetization carried by orbital angular momentum (orbital magnetism), thus bypassing the need for inefficient orbital-to-spin conversion. Recent theoretical studies predict that orbital-orbital interactions can be a sizable fraction of the *s-d* exchange interaction, indicating that the role of orbital exchange could be significant (*30*), which bodes well for the exploration of materials with strong orbital magnetism. Antiferromagnetic (AFM) transition metal oxide insulators can exhibit strong orbital magnetization and at the same time, they exhibit unique properties such as THz spin dynamics (*31, 32*), immunity to external magnetic fields enhancing the stability and low damping, which allows for the transport of angular momentum over long distances (*33, 34*). By making use of the interaction between orbital current from Cu* and unquenched orbital magnetization in CoO, we demonstrate a two orders of magnitude enhancement in the magnetoresistance (MR) in CoO/Cu* bilayers compared to conventional spin-based CoO/Pt. To corroborate that the observed effect originates specifically from the orbital physics and is not a general property of AFM insulators, we measure the MR in α-Fe_2O_3/Cu* bilayers, for which α-Fe_2O_3 exhibits nearly quenched OAM leading to a low conventional MR response (*35*). Our results show that the full efficiency of OHE-based mechanisms can be harnessed when orbital current interacts with local orbital magnetic momentum as found in insulating AFMs.

Results

We use CoO, a collinear insulating AFM, for which the OAM of each Co atom is sizeable ($\approx$ 2.05 μ_B/atom) (*36*), unlike in 3*d* transition metal ferromagnets for which orbital moments are nearly fully quenched due to the crystal field ($<$ 0.1 μ_B/atom) (*37, 38*). The unquenched OAM contributes to both the staggered magnetization and magnetic anisotropies (*39*). Thus CoO serves as an ideal system to investigate the interaction between orbital currents and orbital magnetization and to distinguish it from spin magnetization effects. The insulating nature of CoO is particularly suitable as it allows us to rule out effects of current flow in the magnet such as self-torques or anisotropic MR effects (*40, 41*). The collinear magnetic and crystallographic structure of CoO is

shown in Fig. 1(a).

We deposited epitaxial CoO(5 nm)/Pt(2 nm) and CoO(5 nm)/Cu*(6 nm) thin films on MgO(001) substrates using reactive magnetron sputtering (see supplementary information S1). Here, '*' denotes the natural oxidation of Cu, which serves as an orbital current generator via the OREE (*14*), while Pt generates spin current via the spin Hall effect mechanism (*3*). As shown in Fig. 1(a), the CoO thin films exhibit four-fold in-plane magnetocrystalline anisotropy with two magnetic easy axes of the Néel vector (**n**) oriented along the [110] and [$\bar{1}$10] crystallographic axes (*39, 42, 43*).

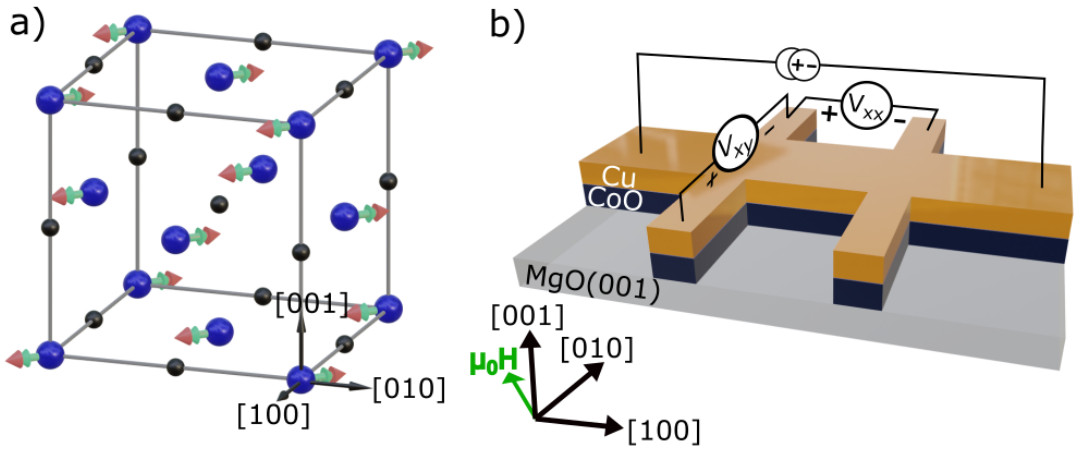

Figure 1: **Magnetic structure of CoO and experimental geometry.** (**a**) Illustration of the magnetic and crystallographic structure of CoO with in-plane magneto-crystalline anisotropy, showing the Néel vector easy axis along the [$\bar{1}$10] axis. The Co and O atoms are represented by blue and black solid circles, respectively. The red and green arrows denote the spin and orbital angular momenta of each Co atom, respectively. (**b**) Schematic of the transverse MR measurement scheme with electrical contacts in the CoO/Cu* structure, including the magnetic field sweep direction [1$\bar{1}$0] shown by a green arrow.

The Néel temperature (T_N) of our thin films is approximately 300 K, slightly higher than that of bulk CoO (T_N = 291 K for bulk CoO (*44, 45*)), which we attribute to the influence of epitaxial strain from the MgO substrate (see supplementary information S1 and S2). Scanning transmission electron microscopy (STEM) and electron energy loss spectroscopy (EELS) confirm the high-quality epitaxial growth of CoO and the formation of sharp, clean and well-defined interfaces in the CoO/Cu* system. Furthermore, the X-ray absorption (XAS) spectroscopy experiments confirm

that our CoO thin films exhibit a very large orbital magnetization (larger than 1 μ_B/atom, see supplementary information S2 and S3).

To investigate the interaction between orbital current and static OAM, we fabricated 6 µm wide Hall bar structures (see Fig. 1(b) for the example of CoO/Cu*) and measured orbital Hall magnetoresistance (OMR) (see Supplementary Information S1). When a charge current I is injected in the Hall bar, it generates orbital current in Cu* via OHE and/or OREE. An orbital accumulation μ_o is then built up at the CoO/Cu* interface. Analogous to the spin Hall magnetoresistance (SMR) mechanism (*46*), the OMR refers to the change in electrical resistance of a non-magnetic material due to the interaction of orbital currents with the magnetization of an adjacent magnetic layer. The change arises from the absorption or reflection of the orbital currents at the interface, depending on the magnetic configuration of the AFM, which in our case is governed by the orientation of the Néel vector.

Although SMR has been studied in Pt adjacent to a range of materials, including 3d ferromagnets and insulating magnets (*46, 47*), the reported pure OMR remains weak for the materials studied (*48*) primarily due to the lack of direct coupling to conventional spin-dominated magnetization in these materials. We first consider a device of CoO/Pt to check the interaction of spin currents with CoO to compare it to the interaction of orbital currents in CoO/Cu*. Initially, we apply an external magnetic field of 13 T along the [110] direction of CoO to align the Néel vector along the well-defined $[\bar{1}10]$ magnetic easy axis (*42*). We then sweep the magnetic field in $[\bar{1}10]$ direction and probe the orientation of Néel vector by measuring the transverse resistance (R_{xy}) at $T(< T_N) = 150$ K. R_{xy} exhibits different behavior when the magnetic field is swept upward and downward in the range of $7.5 - 9$ T as shown in Fig. 2(a). This change in R_{xy}, normalized by the longitudinal resistance, represents the spin-flop transition and rotation of the Néel vector by 90° i.e. from $[\bar{1}10]$ to [110] in this case. The orientation of the Néel vector remains unchanged upon reducing the magnetic field to zero (*42*). Therefore, the difference in R_{xy} at zero fields, before and after the magnetic field sweep, effectively probes the two perpendicular Néel vector orientations, providing a measure of SMR amplitudes. Furthermore, since the SMR is estimated from resistance measurements taken at zero magnetic fields, additional contributions to the MR from the metallic layers, such as Hanle magnetoresistance (*49*), can be ruled out. The amplitude of SMR ($\Delta R_{xy}/\bar{R}$) in CoO/Pt at 150 K is found to be 0.0078%. This amplitude of the SMR is in the order of what is found for all

combinations of Pt with magnetic insulators with spin-based magnetization such as NiO, YIG and hematite (*46, 50, 51*). Based on the theory of SMR in magnetic insulators, the spin Hall angle (θ_{SH}) of 2 nm thick Pt, with a resistivity of 26 μΩcm at 150 K, is estimated to be ≈ 3.5 % with spin diffusion length $\lambda_s \approx 1.5$ nm, which agrees well with previous studies (*42*). Here, we use a literature value for the real part of the spin-mixing conductance to be $G_r = 5 \times 10^{14}\,\Omega^{-1}\mathrm{m}^{-2}$ (*46*).

As the first key result, we now compare this to OMR measurements on the CoO/Cu* sample. Figure 2(b) shows the transverse resistance R_{xy}, normalized by the longitudinal resistance, as a function of the magnetic field measured at $T = 150$ K (below T_{N}). The magnetic field protocol used is the same as that for the measurements in Fig. 2(a). An abrupt change in R_{xy} is observed at the spin-flop field, which occurs at approximately 7.5 − 9 T. This value is similar to that observed for CoO/Pt, indicating that the magneto-crystalline anisotropy of CoO remains largely unaffected by the choice of metallic layer on top. The observation of MR in the absence of any significant spin current source indicates the presence of orbital currents originating from Cu*, consistent with previous observations of OMR in Cu* adjacent to metallic ferromagnets (*48*). Most importantly, we observe a change in the sign of R_{xy} at the spin-flop field compared to the CoO/Pt structure. This result represents a unique characteristic of orbital current interaction with the unquenched orbital moment in CoO. Such an interaction has not been reported in previous studies on 3*d* transition metal ferromagnets with quenched OAM (*48*). The most striking result is the OMR magnitude of 0.28%, which is approximately *36* times larger than the SMR observed in CoO/Pt.

Although Cu* has been recently identified as an efficient source of orbital current (*14, 27*), the observed two orders of magnitude higher MR in CoO/Cu* cannot be explained solely by the large orbital currents, as the magnitude of OMR in our previous results for NiFe/Cu* (0.05 %) is found to be significantly smaller than the OMR in our CoO/Cu* (*48*). Furthermore, torque experiments reveal that the torques on magnetic layers in which the OAM is quenched, are not enhanced by the here observed two orders of magnitude since the orbital currents from Cu* need to be converted into spin currents via the weak SOC of Pt (*14, 27*).

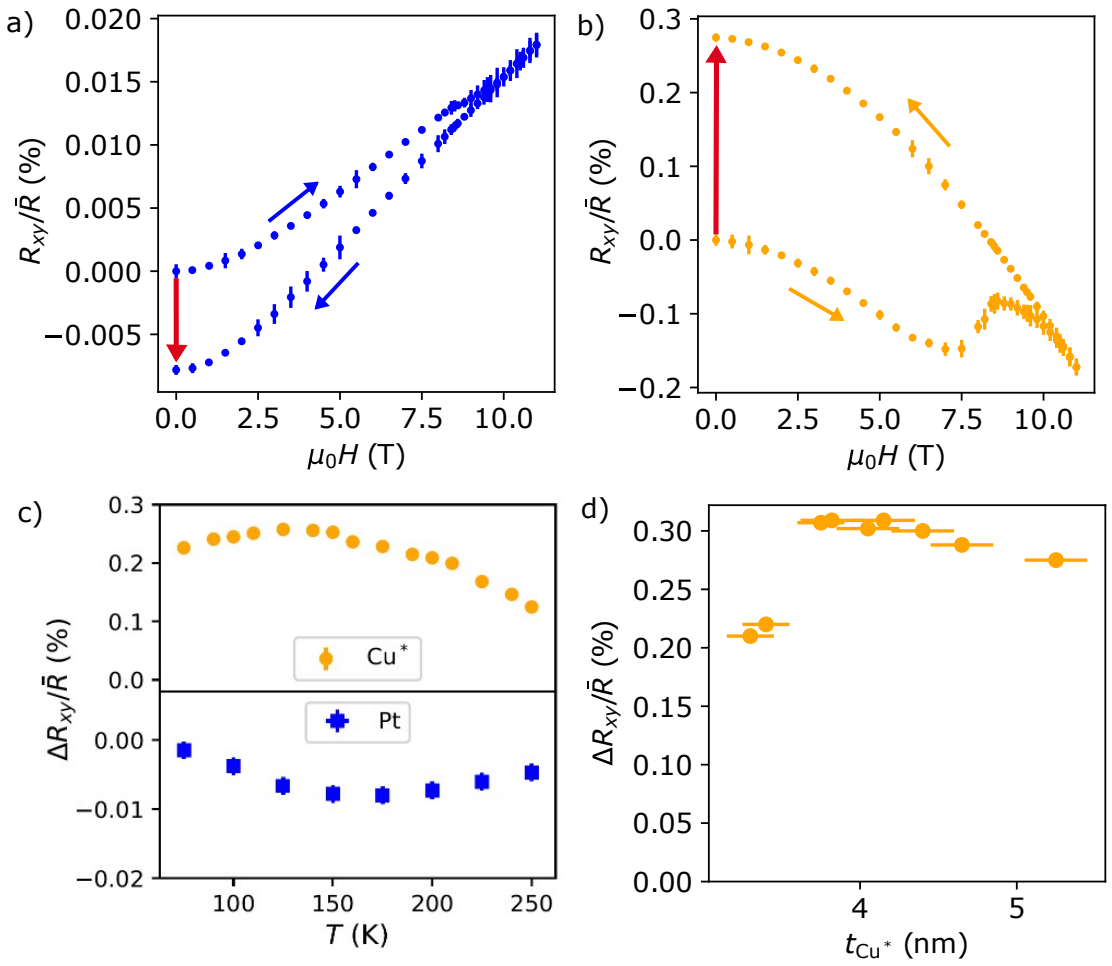

Figure 2: **Spin and orbital Hall magnetoresistance**. Magnetic field-sweep measurements on (**a**) CoO(5 nm)/Pt(2 nm) and (**b**) CoO(5 nm)/Cu*(6 nm) samples, respectively. Both samples exhibit a spin-flop transition between 7.5 T – 9 T. The change in transverse resistance corresponding to the two perpendicular Néel vector orientations is indicated by the red arrow for SMR in **a** and OMR in **b**. The measurements are performed at $T = 150$ K. (**c**) The difference in transverse resistance, normalized with the longitudinal resistance for two perpendicular Néel vector states at zero field as a function of temperature. The top panel presents the results for CoO/Cu* (in yellow), while the bottom panel shows the results for CoO/Pt (in blue). (**d**) The difference in transverse resistance for two perpendicular Néel vector states at zero field as a function of Cu-layer thickness in CoO/Cu*(t). The measurements were performed at a constant temperature of $T = 150$ K.

Our experimental results thus suggest that additional factors or mechanisms must contribute to

the giant amplitude of the MR in the CoO/Cu* system. Specifically, our findings provide strong evidence that while spin currents from Pt interact with the spin magnetization in CoO via spin exchange coupling, the orbital current from Cu* interacts strongly with the large unquenched component of the orbital magnetization in CoO. This interaction is dominant in CoO/Cu* samples in which no significant source of spin current is present, and is thus responsible for the giant OMR compared to the conventional CoO/Pt. To validate this interpretation, we compare the results to the MR in α-Fe_2O_3/Cu*, for which the static OAM is quenched and does not contribute significantly to the magnetization of α-Fe_2O_3 (see Supplementary Information S5). The results show that the OMR is nearly absent in the α-Fe_2O_3/Cu* system, and since the insulating nature of the magnet does not allow for orbital to spin conversion, no SMR is expected, thus supporting our interpretation.

We next comment on the opposite sign of MR in the two systems. The sign of spin current from Pt and orbital current from Cu* is theoretically predicted (*21*) and experimentally found to be the same, as confirmed by the same sign of SMR and OMR in NiFe/Pt and NiFe/Cu* systems (*48*). The unquenched OAM of CoO can give rise to an orbital quadrupole moment. Our results indicate that the dynamics of the orbital quadrupole moment in CoO are fundamentally different from the classical dynamics of ferromagnets. A similar anomaly in quadrupole moment dynamics has recently been experimentally demonstrated (*52*).

To understand the underlying mechanisms for the large MR magnitude and its sign, we compare the temperature dependence of the MR in the two systems. Figure 2(c) shows the evolution in MR as a function of temperature in CoO/Cu* (top panel) and CoO/Pt (bottom panel). The sign of MR in CoO/Cu* remains opposite to that of CoO/Pt throughout the measured temperature range, however, the magnitude does vary. In CoO/Cu*, the MR signal increases initially, from 0.15% at 275 K to a peak of 0.28% at 150 K, followed by a slight decrease as the temperature is further lowered to 75 K. For comparison, we also measured the temperature dependence of MR in CoO/Pt, which shows a similar temperature trend, but with an opposite sign and a two-order of magnitude lower amplitude if compared to CoO/Cu*. Remarkably, the amplitude of MR in CoO/Cu* sample compared to the CoO/Pt sample increases further at lower temperatures. At $T = 200$ K, MR in CoO/Cu* is a factor 35 larger than the CoO/Pt. At $T = 100$ K the ratio increases to a factor of *64*. Although a similar temperature dependence has been previously observed in studies of SMR and torques in YIG/Pt bilayers (*51*), as well as in ferromagnetic/Pt bilayers, the increase in the

ratio of OMR in CoO/Cu* to SMR in CoO/Pt suggests that two different mechanisms are involved. We attribute this temperature dependence primarily to angular momentum relaxation mediated by phonon scattering, which likely plays a significant role (*51*) for SMR but orbital angular momentum is not prone to these damping mechanisms.

The observed orbital current could have its origin primarily in either the bulk Cu* via OHE or at the surface via OREE. To determine the origin, we perform Cu* thickness-dependent measurements of OMR in CoO/Cu*(t) samples at 150 K. To investigate this within the same device, i.e. keeping the CoO/Cu* interface unchanged, we progressively reduce the Cu* layer thickness using a Ar^+ ion milling technique, followed by exposure to air for 12 hours after each etching step. The remaining Cu* thickness after each etching step was estimated by comparing the sheet resistance of the milled device to that of separately grown Cu*(t) thin films (see Supplementary Information S6). In Fig. 2(d), we show the Cu* layer thickness dependence of the OMR. The results reveal that the OMR nearly remains constant at approximately 0.32 % for Cu* thicknesses ranging from 3.7 to 5.5 nm. When the Cu* thickness is reduced further to 3.2 nm, the OMR decreases slightly, from 0.32 % to 0.22 %. For Cu* thicknesses below 3.2 nm, the sample becomes insulating, making it impossible to measure any OMR. This observed trend suggests that the orbital current responsible for the OMR in our samples predominantly originates at the surface of the Cu layer, for which we find a pronounced oxidation (see supplementary information S2 for the detailed EELS data), likely facilitated by an OREE. The gigantic enhancement of OMR observed can thus result from the efficient generation of large orbital currents at the oxidized Cu surface by OREE. Furthermore, the nearly constant OMR in the thickness range of 3.7 to 5.5 nm implies that this mechanism is robust within this thickness regime, likely due to sufficient Cu volume and thus constant oxygen gradient and Cu* thickness. This supports the orbital current generation and transport and makes it more suitable for applications.

To determine whether the observed effect originates from the CoO layer and to rule out contributions from other effects, such as the Hanle effect and Lorentzian magnetoresistance in metallic layers, we measure the angular-dependence of R_{xy} for different magnetic field amplitudes. The magnetic field strengths range from values below to above the spin-flop fields of CoO. We extract the MR amplitude as detailed in Supplementary Text S7. Figure 3 shows that the amplitude of the MR is nearly zero for magnetic field strengths below the spin-flop transition for both samples. As the

magnetic field is increased beyond the spin-flop field (8˘9 T), the MR signal saturates, confirming that the observed effect is field-independent and ruling out the contribution from other spurious signal origins. The amplitude of the MR measured is consistent with the values obtained using the zero-field approach (see Fig. 2(c)) at $T = 200$ K, showing the robustness of our measurement approach and the effect. Additionally, the observed hysteresis in the transverse MR is in line with the presence of significant unquenched OAM in our sample (*39*).

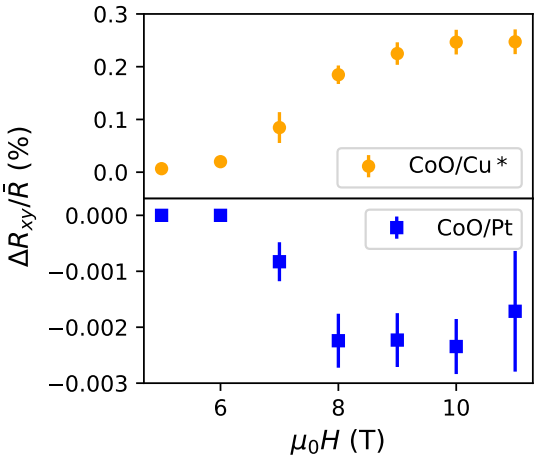

Figure 3: **External field dependence of MR.** The change in transverse MR for CoO(5 nm)/Cu*(6 nm) and CoO(5 nm)/Pt(2 nm) as a function of applied magnetic field at $T = 200$ K.

Discussion and outlook

CoO is known for its uncompensated atomic-like orbital magnetism of d-electrons which arises as a result of a combination between the crystal field, band filling and electron-electron correlation of t_{2g}-electrons, see e.g. (*53, 54*). Our first-principles calculations of the AFM CoO for experimental lattice parameters predict the value of the gap of the order of 2.5 eV, with the magnitude of local spin and orbital moments of the order of 2.70 μ_B and 1.2 μ_B (see supplementary information S3 and S8). The spin and orbital moments preserve their magnitude once the effect of spin-orbit coupling is gradually switched off in electronic structure calculations. While the spin degree of freedom is coupled to the orbital moments via relatively weak spin-orbit interaction, the effect of significant orbital splitting among the states with opposite orbital polarization, which accounts for the order of

the band gap, can be perceived in the orbital channel only as a result of an effective orbital exchange term in the Hamiltonian which signifies the repulsion energy between orbitally-polarized states.

To probe the response properties of CoO to injected spin and orbital currents, we perform first-principles linear response calculations (see supplementary information S9 for the details) of the spin and orbital moments, S_i and L_i, as well as orbital quadrupoles $\{L_i, L_j\}$, induced by applied spin and orbital exchange fields, which can mimic the effect of spin and orbital currents on the electronic structure of bulk CoO in case of CoO/Pt and CoO/Cu* interfaces. The calculations of the corresponding response tensors for the [110] and [1$\bar{1}$0] directions of the Néel vector within the band gap of CoO (see Figs. S11 and S12) for details), reveal that the response to the induced orbital fields is orders of magnitude larger than for the case of spin exchange fields – an effect which clearly originates in the unquenched orbital momentum of Co atoms. Moreover, the spin and orbital response tensors exhibit a much stronger anisotropy with respect to the direction of $\hat{\boldsymbol{n}}$ when perturbed by the orbital field, while the response to the injected spin is only very weakly anisotropic. This is to be expected, since the response to the orbital perturbation directly feeds off the intrinsic anisotropy of the magnetic structure in CoO as reflected e.g. in the sensitivity of the orbital moments and crystal field splittings on the direction of $\hat{\boldsymbol{n}}$, that we observe in our calculations. Overall, we can make a conclusion that promoting the spin and orbital dynamics by exploiting orbital injection from CoO/Cu* interface results in more complex, more anisotropic and more pronounced dynamical response of the intertwined system of Co spin and orbital moments.

In contrast to spin, the strong orbital response of CoO to injected orbital angular momentum can result in the giant OMR amplitude e.g. via modifications in the anisotropy profile brought by the large non-vanishing current-induced orbital quadrupoles $\langle\{L_i, L_j\}\rangle$. Recently, the currents of orbital quadrupole moments coupled to spin by spin-orbit interaction of Pt have been shown to mediate an injection of magnetic octupole into altermagnetic materials, thereby driving a novel type of torque on the Néel order parameter $\hat{\boldsymbol{n}}$ originated in the linear coupling between $\hat{\boldsymbol{n}}$ and the magnetic octupole moment (*55*). In CoO, it has been recently shown that the orbital quadrupole moment, arising as a combined result of an externally applied magnetic field and spin-orbit interaction, plays a key role in driving intricate spin-orbital dynamics via the term in energy which couples components of $\hat{\boldsymbol{n}}$ and $\langle\{L_x, L_y\}\rangle$ (*39*). We can show (see supplementary information S10 that due to the coupling with the spins, the induced quadrupole moment generates a strongly anisotropic

torque on the Néel vector, thus inducing coupled spin-orbital dynamics resulting in energy losses and an increase in the MR signal. Since the orbital dipole-to-quadrupole conversion does not in principle require spin-orbit interaction, we believe that the effective orbital quadrupole torques originating from the orbital injection from Cu* can be very efficient and ultimately result in strong absorption of the electrically-generated OAM. Note that the large values of orbital moment and orbital quadrupoles in CoO are key in generating such kind of torques.

One remarkable feature of CoO, as compared to other materials of this kind, are strong orbital exchange interactions. To demonstrate this, we perform explicit ab-initio calculations of spin and orbital dipole and quadrupole exchange couplings in CoO (see supplementary information S11). We find that isotropic antiferromagnetic next-nearest-neighbor spin-spin exchange interaction is by far the largest (about 90 meV). However, among the nearest-neighbor exchange interactions, the largest magnitudes are found within the orbital quadrupole-quadrupole subblock, with the largest coupling of the order of 12 meV. This provides an additional purely orbital channel for energy dissipation by low-energy excitations of orbital degrees of freedom when corresponding dynamics is triggered by the orbital current generated at the CoO/Cu* interface. To show this, we consider the absorptive part of the susceptibility of CoO, and compute it along high-symmetry directions of the parent fcc Brillouin zone (for details see Fig. S14). We find that within the considered range, two wide groups of excitation bands are present, with the lower one residing between 20 and 45 meV, the upper band is reaching out beyond 60 meV. While the exact energetic position of the excitation bands depends sensitively on the structural details of the film and its interfacial properties, the relative difference in the energy of the lower and upper group stems from the qualitatively different nature of the interactions that define them. Indeed, we identify that the lower band is mainly of orbital-quadrupole character, while the upper one is mainly due to spin excitations. Therefore, the efficient mechanism of orbital excitations by the orbital current, in addition to discussed above coherent torques exerted on the Néel order, can also contribute to a much stronger orbital current absorption by CoO in the Cu* system than that related to spin current-driven dynamics in Pt-based bilayers thus explaining the experimental observation.

As a final remark, the demonstrated two-orders-of-magnitude enhancement in magnetoresistance in the CoO/Cu* system compared to conventional CoO/Pt has wide repercussions. To check the universality of the observation, we have replaced Cu* by Cr as another system that can generate

large orbital angular momentum. We find that using this metal with weak SOC and a negligible spin Hall effect, a 5 times larger signal is observed in CoO/Cr than CoO/Pt (for details see supplementary information S4). This underscores the applicability of our discovered mechanism and highlights the potential of giant orbital currents to efficiently detect and potentially also manipulate magnetic order via this novel route. For applications, materials with higher ordering temperature than our CoO and in particular orbital angular momentum dominating ferro- and ferrimagnets will be particularly apt. Overall, the interaction mechanisms that arise from the combination of the giant orbital current generated in Cu* and Cr and the large unquenched static OAM in orbital magnets such as the CoO used here, could enable the development of all-orbital devices overcoming the limitations of conventional SOC mediated processes.

Literatura

1. M. N. Baibich, *et al.*, Giant Magnetoresistance of (001)Fe/(001)Cr Magnetic Superlattices. *Phys. Rev. Lett.* **61**, 2472–2475 (1988).

2. G. Binasch, P. Grünberg, F. Saurenbach, W. Zinn, Enhanced magnetoresistance in layered magnetic structures with antiferromagnetic interlayer exchange. *Phys. Rev. B* **39**, 4828–4830 (1989).

3. I. M. Miron, *et al.*, Perpendicular switching of a single ferromagnetic layer induced by in-plane current injection. *Nature* **476** (7359), 189–193 (2011).

4. S. Bhatti, *et al.*, Spintronics based random access memory: a review. *Mater. Today* **20** (9), 530–548 (2017).

5. A. Fert, V. Cros, J. Sampaio, Skyrmions on the track. *Nat. Nanotechnol.* **8** (3), 152–156 (2013).

6. K. Everschor-Sitte, J. Masell, R. M. Reeve, M. Kläui, Perspective: Magnetic skyrmions—Overview of recent progress in an active research field. *J. Appl. Phys.* **124** (24), 240901 (2018).

7. X. Zhang, M. Ezawa, Y. Zhou, Magnetic skyrmion logic gates: conversion, duplication and merging of skyrmions. *Sci. Rep.* **5** (1), 9400 (2015).

8. J. Grollier, *et al.*, Neuromorphic spintronics. *Nat. Electron.* **3** (7), 360–370 (2020).

9. T. da Câmara Santa Clara Gomes, *et al.*, Neuromorphic weighted sums with magnetic skyrmions. *Nat. Electron.* **8** (3), 204–214 (2025).

10. G. Beneke, *et al.*, Gesture recognition with Brownian reservoir computing using geometrically confined skyrmion dynamics. *Nat. Commun.* **15** (1), 8103 (2024).

11. A. Manchon, *et al.*, Current-induced spin-orbit torques in ferromagnetic and antiferromagnetic systems. *Rev. Mod. Phys.* **91**, 035004 (2019).

12. D. Go, D. Jo, H.-W. Lee, M. Kläui, Y. Mokrousov, Orbitronics: Orbital currents in solids. *Europhys. Lett.* **135** (3), 37001 (2021).

13. D. Go, D. Jo, C. Kim, H.-W. Lee, Intrinsic Spin and Orbital Hall Effects from Orbital Texture. *Phys. Rev. Lett.* **121**, 086602 (2018).

14. S. Ding, *et al.*, Harnessing Orbital-to-Spin Conversion of Interfacial Orbital Currents for Efficient Spin-Orbit Torques. *Phys. Rev. Lett.* **125**, 177201 (2020).

15. K.-J. Lee, V. Cros, H.-W. Lee, Electric-field-induced orbital angular momentum in metals. *Nat. Mater.* **23** (10), 1302–1304 (2024).

16. T. Tanaka, *et al.*, Intrinsic spin Hall effect and orbital Hall effect in 4*d* and 5*d* transition metals. *Phys. Rev. B* **77**, 165117 (2008).

17. H. Kontani, T. Tanaka, D. S. Hirashima, K. Yamada, J. Inoue, Giant Orbital Hall Effect in Transition Metals: Origin of Large Spin and Anomalous Hall Effects. *Phys. Rev. Lett.* **102**, 016601 (2009).

18. A. Johansson, B. Göbel, J. Henk, M. Bibes, I. Mertig, Spin and orbital Edelstein effects in a two-dimensional electron gas: Theory and application to $SrTiO_3$ interfaces. *Phys. Rev. Res.* **3**, 013275 (2021).

19. S. A. Nikolaev, *et al.*, Large Chiral Orbital Texture and Orbital Edelstein Effect in Co/Al Heterostructure. *Nano Lett.* **24** (43), 13465–13472 (2024).

20. A. Fert, R. Ramesh, V. Garcia, F. Casanova, M. Bibes, Electrical control of magnetism by electric field and current-induced torques. *Rev. Mod. Phys.* **96**, 015005 (2024).

21. L. Salemi, P. M. Oppeneer, First-principles theory of intrinsic spin and orbital Hall and Nernst effects in metallic monoatomic crystals. *Phys. Rev. Mater.* **6** (9), 095001 (2022).

22. S. Krishnia, *et al.*, Large Interfacial Rashba Interaction Generating Strong Spin–Orbit Torques in Atomically Thin Metallic Heterostructures. *Nano Lett.* **23** (15), 6785–6791 (2023).

23. Y.-G. Choi, *et al.*, Observation of the orbital Hall effect in a light metal Ti. *Nature* **619** (7968), 52–56 (2023).

24. I. Lyalin, S. Alikhah, M. Berritta, P. M. Oppeneer, R. K. Kawakami, Magneto-Optical Detection of the Orbital Hall Effect in Chromium. *Phys. Rev. Lett.* **131**, 156702 (2023).

25. J. C. Idrobo, *et al.*, Direct observation of nanometer-scale orbital angular momentum accumulation. *arXiv preprint* (2024), 2403.09269.

26. A. Bose, *et al.*, Detection of long-range orbital-Hall torques. *Phys. Rev. B* **107**, 134423 (2023).

27. S. Krishnia, *et al.*, Quantifying the large contribution from orbital Rashba–Edelstein effect to the effective damping-like torque on magnetization. *APL Mater.* **12** (5), 051105 (2024).

28. G. Sala, P. Gambardella, Giant orbital Hall effect and orbital-to-spin conversion in $3d$, $5d$, and $4f$ metallic heterostructures. *Phys. Rev. Res.* **4**, 033037 (2022).

29. R. Gupta, *et al.*, Harnessing orbital Hall effect in spin-orbit torque MRAM. *Nat. Commun.* **16** (1), 130 (2025).

30. M. I. Katsnelson, Y. O. Kvashnin, V. V. Mazurenko, A. I. Lichtenstein, Correlated band theory of spin and orbital contributions to Dzyaloshinskii-Moriya interactions. *Phys. Rev. B* **82**, 100403 (2010).

31. E. Rongione, *et al.*, Emission of coherent THz magnons in an antiferromagnetic insulator triggered by ultrafast spin-phonon interactions. *Nat. Commun.* **14** (1), 1818 (2023).

32. T. Kampfrath, *et al.*, Coherent terahertz control of antiferromagnetic spin waves. *Nat. Photonics* **5** (1), 31–34 (2011).

33. R. Lebrun, *et al.*, Tunable long-distance spin transport in a crystalline antiferromagnetic iron oxide. *Nature* **561** (7722), 222–225 (2018).

34. S. Das, *et al.*, Anisotropic long-range spin transport in canted antiferromagnetic orthoferrite $YFeO_3$. *Nat. Commun.* **13** (1), 6140 (2022).

35. G. Rollmann, A. Rohrbach, P. Entel, J. Hafner, First-principles calculation of the structure and magnetic phases of hematite. *Phys. Rev. B* **69** (16), 165107 (2004).

36. M. Norman, Orbital polarization and the insulating gap in the transition-metal oxides. *Phys. Rev. Lett.* **64** (10), 1162 (1990).

37. C. T. Chen, *et al.*, Experimental Confirmation of the X-Ray Magnetic Circular Dichroism Sum Rules for Iron and Cobalt. *Phys. Rev. Lett.* **75**, 152–155 (1995).

38. S. Krishnia, *et al.*, Interfacial spin-orbitronic effects controlled by different oxidation levels at the Co/Al interface. *Phys. Rev. Appl.* **24**, 024055 (2025).

39. M. Grzybowski, *et al.*, Antiferromagnetic hysteresis above the spin-flop field. *Phys. Rev. B* **107** (6), L060403 (2023).

40. W. Wang, *et al.*, Anomalous spin-orbit torques in magnetic single-layer films. *Nat. Nanotech.* **14** (9), 819–824 (2019).

41. S. Krishnia, *et al.*, Spin-Orbit Coupling in Single-Layer Ferrimagnets: Direct Observation of Spin-Orbit Torques and Chiral Spin Textures. *Phys. Rev. Appl.* **16**, 024040 (2021).

42. L. Baldrati, *et al.*, Efficient spin torques in antiferromagnetic CoO/Pt quantified by comparing field-and current-induced switching. *Phys. Rev. Lett.* **125** (7), 077201 (2020).

43. C. Schmitt, *et al.*, Mechanisms of Electrical Switching of Ultrathin CoO/Pt Bilayers. *Nano Lett.* **24** (5), 1471–1476 (2024).

44. W. Roth, Magnetic structures of MnO, FeO, CoO, and NiO. *Phys. Rev.* **110** (6), 1333 (1958).

45. S. Saito, K. Nakahigashi, Y. Shimomura, X-ray diffraction study on CoO. *J. Phys. Soc. Jpn.* **21** (5), 850–860 (1966).

46. H. Nakayama, *et al.*, Spin Hall Magnetoresistance Induced by a Nonequilibrium Proximity Effect. *Phys. Rev. Lett.* **110**, 206601 (2013).

47. J. Kim, P. Sheng, S. Takahashi, S. Mitani, M. Hayashi, Spin Hall Magnetoresistance in Metallic Bilayers. *Phys. Rev. Lett.* **116**, 097201 (2016).

48. S. Ding, *et al.*, Observation of the Orbital Rashba-Edelstein Magnetoresistance. *Phys. Rev. Lett.* **128**, 067201 (2022).

49. S. Vélez, *et al.*, Hanle magnetoresistance in thin metal films with strong spin-orbit coupling. *Phys. Rev. Lett.* **116** (1), 016603 (2016).

50. G. R. Hoogeboom, A. Aqeel, T. Kuschel, T. Palstra, B. J. van Wees, Negative spin Hall magnetoresistance of Pt on the bulk easy-plane antiferromagnet NiO. *Appl. Phys. Lett.* **111** (5) (2017).

51. S. R. Marmion, M. Ali, M. McLaren, D. A. Williams, B. J. Hickey, Temperature dependence of spin Hall magnetoresistance in thin YIG/Pt films. *Phys. Rev. B* **89**, 220404 (2014).

52. J.-Y. Yoon, *et al.*, Handedness anomaly in a non-collinear antiferromagnet under spin–orbit torque. *Nat. Mater.* **22** (9), 1106–1113 (2023).

53. I. V. Solovyev, A. I. Liechtenstein, K. Terakura, Is Hund's Second Rule Responsible for the Orbital Magnetism in Solids? *Phys. Rev. Lett.* **80**, 5758–5761 (1998).

54. A. Boussendel, N. Baadji, A. Haroun, H. Dreyssé, M. Alouani, Effect of substrate strain on calculated magnetic properties and magnetic anisotropy energy of CoO. *Phys. Rev. B* **81**, 184432 (2010).

55. S. Han, *et al.*, Harnessing magnetic octupole Hall effect to induce torque in altermagnets. *Phys. Rev. Lett.* **135** (7), 076705 (2025).

Acknowledgments

We acknowledge fruitful discussions with Daegeun Jo and Kyun-Jin Lee. We thank D. A. Grave, A. Kay and A. Rothschild for providing us with the α-Fe_2O_3 thin film. We thank HZB for the allocation of synchrotron radiation beam time, and we thankfully acknowledge the financial support by HZB. The authors thank the DFG (Spin+X (A01, A11, B02) TRR 173-268565370 and Project No. 358671374), the Horizon 2020 Framework Programme of the European Commission under FETOpen Grant Agreement No. 863155 (s-Nebula); the European Research Council Grant Agreement No. 856538 (3D MAGiC); and the Research Council of Norway through its Centers of Excellence funding scheme, Project No. 262633 "QuSpin". This project has received funding from the EU Research and Innovation Programme Horizon Europe under grant agreement No. 101070290 (NIMFEIA). We also gratefully acknowledge the Jülich Supercomputing Centre for

providing computational resources under projects jiff40 and jiff38. The study also has been supported by the European Horizon Europe Framework Programme under an EC Grant Agreement N°101129641 ”OBELIX”. This research is part of the TOPOCOM project, which is funded by the European Union's Horizon Europe Programme under the Marie Skłodowska-Curie Actions (MSCA), Grant Agreement No. 101119608. The work at the University of Tokyo was supported by CREST (Nos. JPMJCR20C1 and JPMJCR20T2) from JST, Japan, Grant-in-Aid for Scientific Research (S) (No. JP19H05600), Grant-in-Aid for Transformative Research Areas (No. JP22H05114) from JSPS KAKENHI, Japan, Grant-in-Aid for Scientific Research (B) (No. JP24K01326), Grant-in-Aid for Research Activity Start-up (No. 23K19024) from JSPS KAKENHI, Japan, Institute for AI and Beyond of the University of Tokyo, and Sumitomo Chemical. O.G. and J.S. acknowledge support of DFG (Elasto-Q-Mat, TRR 288 – 422213477 projects A12 and A09).

Author contributions: The CoO samples were grown by CS and LM with the assistance of TKi and HA supervised by ES. CS fabricated the devices and performed the electrical measurements. SK and EG assisted with the experiments. CS and SK analyzed the data with inputs from TKu, YM, GJ and MK. TD and AK acquired and analyzed the TEM data supervised by RD. CS, EG, MLo and JK performed the XAS measurements, supported by FK. MZ, MLe, DG, LVP, JS, OG and YM provided the theoretical support. RX performed supporting electrical measurements. DT helped in the sputtering of metal layers. CS, SK, LVP, YM and MK wrote the manuscript. MK proposed and supervised the whole project. All authors commented on the manuscript.

Competing interests: The authors declare no competing interests.

Data and materials availability: The data is available from the corresponding author on reasonable request.